Capillary instabilities in thin nematic liquid crystalline fibers

Ae-Gyeong Cheong and Alejandro D. Rey*
Department of Chemical Engineering, McGill University, 3610 University Street, Montreal, Quebec, Canada H3A 2B2

Patrick T. Mather
University of Connecticut, Institute of Materials Science, Polymer Program, 97 North Eagleville Road, U-136, Storrs, Connecticut 06269-3136

(Received 22 December 2000; revised manuscript received 24 May 2001; published 21 September 2001)

A complete identification and characterization of three distinct capillary instabilities in nematic liquid crystal fibers is presented. Linear stability analysis of capillary instabilities in thin nematic liquid crystalline cylindrical fibers is performed by formulating and solving the governing nematocapillary equations. A representative axial nematic orientation texture is studied. The surface disturbance is expressed in normal modes, which include the azimuthal wavenumber *m* to take into account nonaxisymmetric modes of the disturbance. Capillary instabilities in nematic fibers reflect the anisotropic nature of liquid crystals, such as the orientation contribution to the surface elasticity and surface bending stresses. Surface gradients of bending stresses provide additional anisotropic contributions to the capillary pressure that may renormalize the classical displacement and curvature forces that exist in any fluid fiber. The exact nature (stabilizing and destabilizing) and magnitude of the renormalization of the displacement and curvature forces depend on the nematic orientation and the anisotropic contribution to the surface energy, and accordingly capillary instabilities may be axisymmetric or nonaxisymmetric, with finite or unbounded wavelengths. Thus, the classical fiber-to-droplet transformation is one of several possible instability pathways while others include surface fibrillation.

DOI: 10.1103/PhysRevE.64.041701 PACS number(s): 61.30.Hn, 68.03.Kn, 68.03.Cd

I. INTRODUCTION

The current wide use of thin fibers, films and multiphase material systems demands a fundamental understanding of capillary hydrodynamics, interfacial thermodynamics, and interfacial transport phenomena [1–3]. Many new liquid crystal applications involving strong interfacial effects such as mesophase fiber spinning [4] and formation of *in situ* liquid crystal polymer composites [5] also require a fundamental understanding of capillary hydrodynamics. Despite a good understanding of interfacial liquid crystal thermodynamics [6–14], nonequilibrium surface phenomena are not well understood and/or characterized. Force balance equations describing static [15–20] and dynamical interfacial phenomena [17,20] are available but have not been widely used in describing the mechanics of fiber and film microstructures. This paper is concerned with the mechanics and stability of thin nematic liquid crystalline fibers.

A question of fundamental importance in capillary instabilities of thin fibers is the nature of the modes that arise as driven by surface tension forces. In isotropic fluid fibers, the fiber-to-droplet transformation is well understood and known as the fiber Rayleigh instability [1,2,21]. In this case, displacement capillary forces drive the fiber break-up, while curvature dependent forces resist the instability. Since in these materials surface tension is isotropic, only axisymmetric mode emerges, eventually generating spherical droplets. On the other hand, an essential characteristic of nematic liquid crystals is mechanical anisotropy [22]. The anisotropies in the viscoelastic bulk properties of nematic liquid crystal are well understood theoretically [23,24] and experimentally [22], and the anisotropies in the surface elastic properties of nematics are also well-characterized [7,9]. It is well-known that the surface tension of nematics contains an isotropic contribution as well as an anisotropic contribution, known as the anchoring energy [7,9,22]. The role of anchoring energy on capillary instabilities has been partially studied [5,25] with simplified versions of the governing interfacial linear momentum balance equations. The study of capillary instabilities is based on analysis of macroscopic flow produced by gradients in capillary pressure [1,25]. The capillary pressure is found by projecting the surface gradient of the surface stress tensor along the unit surface normal vector. Thus, the nature of surface stress tensor is at the center of capillary instabilities. For isotropic fluids, the surface stress tensor is a diagonal 2×2 tensor, the capillary pressure is isotropic, and nonaxisymmetric modes on thin cylindrical fibers are thus stable because curvature dampens such costly deformation [2] (isotropic jets, on the other hand, may develop nonaxisymmetric disturbances but only through inertia effects [26–28]). For nematic liquid crystals, the surface stress tensor is a 2×3 tensor, exhibiting both *normal* and *bending* stresses. Bending stresses arise because the surface energy depends on the nematic orientation at the surface. The bending stresses attempt to deform the surface if the surface energy can be lowered in doing so. In this paper, we show that gradients in bending stresses renormalize the capillary pressure effects, creating new axisymmetric and nonaxisymmetric capillary instabilities. The specific objectives of this paper are to (1) derive a general equation that describes capillary instabilities in thin nematic liquid crystal fibers, (2) characterize all the possible capillary instability modes and elucidate the physical mechanisms that drive and quench the instabilities, (3)

*Corresponding Author

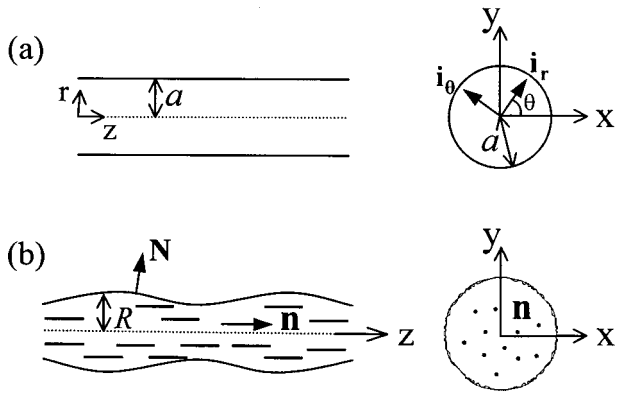

FIG. 1. (a) Unperturbed fiber with radius a is aligned in the z-axis of cylindrical coordinates (r,θ,z). Cross-sectional view in Cartesian coordinates (x, y) shows the unit vectors $\mathbf{i}_r$ and $\mathbf{i}_\theta$ in azimuthal angle θ. (b) Unit surface normal vector **N** and director field $\mathbf{n}(n_z=1)$ of the axial nematic fiber with surface disturbances. Fiber radius R and unit surface normal **N** change along the z and θ directions. In the cross section, the director field **n** is shown as dots and the θ-directional surface disturbances as small-amplitude wrinkles at the surface.

characterize the fundamental role of anisotropic surface elasticity and bending stresses in capillary instabilities, and (4) establish parametric conditions that lead to axisymmetric and nonaxisymmetric capillary instabilities.

The organization of this paper is as follows. In Sec. II, we present the governing nematocapillary equations and derive the instability criteria for a representative nematic texture. In Sec. III, we characterize all possible instability modes and the geometry of the evolving unstable fiber. The instability mechanisms are clearly identified and discussed in terms of capillary forces. All results are summarized in compact tabular form and discussed in detail, emphasizing the physical as well as mathematical aspects. Representative computed visualizations of unstable fibers are included to complement the tabulated and graphical information. Section IV presents conclusions.

II. GOVERNING EQUATIONS

A. Geometry and texture of nematic liquid crystal fibers

To completely define the state of a nematic liquid crystalline fiber, both the geometry of the fiber and the spatial orientational order of the nematic liquid crystal must be specified. More specifically, nematic liquid crystalline fiber $\equiv\{\mathbf{n},R,\mathbf{N}\}$, where **n** is the nematic director field [22], R is the fiber radius, and **N** is the unit surface normal vector. For an isotropic material fiber, only the geometry is necessary, i.e., $\{R,\mathbf{N}\}$.

Figure 1 shows definitions of the fiber geometry and nematic texture. Figure 1(a) shows that the fiber is initially a uniform cylinder with radius a, and the fiber axis is collinear with the z axis of a cylindrical coordinate system. The fiber nematic texture is expressed by the director field using unit vectors $\mathbf{i}_r$, $\mathbf{i}_\theta$, and $\mathbf{i}_z$ in the direction of the r, θ, and z axes, respectively. In this paper, we restrict our analysis to a nematic texture with a fixed director field, denoted as axial texture, and the nematic fiber with the axial texture is called ''axial fiber.'' Figure 1(b) shows the axial fiber with surface disturbances. In the cross-sectional view of Fig. 1(b), the director field **n** is shown as dots and the θ-directional surface disturbances as small-amplitude wrinkles at the surface, although in real the surface noise is too small to be visually detected. The fiber radius R and the unit surface normal **N** change along the z and θ directions. In the axial texture, the director is oriented along the fiber axis and it is given by

$$\mathbf{n}=\mathbf{i}_z. \tag{1}$$

The fiber shape at any time t and position z and θ is given by

$$R(z,\theta,t)=a+\xi(z,\theta,t). \tag{2}$$

The surface disturbance ξ is expressed in a harmonic series

$$\xi(z,\theta,t)=\sum\ \xi_0 e^{\alpha t+i(kz+m\theta)}, \tag{3}$$

where ξ_0 is the initial amplitude of the disturbance, α the growth rate for real and positive values, k the axial wave number, and m the azimuthal wave number. The wave vector (k, m) is composed of two wave numbers. Due to rotational periodicity, the azimuthal wave number m is an integer and specifies the disturbance mode in the azimuthal (θ) direction. Axisymmetric modes correspond to $m=0$, while nonaxisymmetric modes correspond to $m\neq 0$. During a capillary instability the fiber geometry evolution is captured by the fiber's radius (R), the principal radii of curvature $(R_{r\theta},R_{rz})$, and its unit surface normal $(\mathbf{N})$. To discuss capillary instabilities it is also useful to introduce the following expression for the mean curvature H in cylindrical coordinates

$$\begin{aligned}H&=-\frac{1}{2}\boldsymbol{\nabla}_s\cdot\mathbf{N}=-\frac{1}{2}\left(\frac{1}{R_{r\theta}}+\frac{1}{R_{rz}}\right)\\&=\frac{-1}{2\sqrt{\left(1+\dfrac{R_{,\theta}^2}{R^2}+R_{,z}^2\right)^3}}\left[\frac{1}{R}\left(1+\frac{2R_{,\theta}^2}{R^2}+R_{,z}^2\right)\right.\\&\quad\left.-(1+R_{,z}^2)\frac{R_{,\theta\theta}}{R^2}-\left(1+\frac{R_{,\theta}^2}{R^2}\right)R_{,zz}+\frac{2}{R^2}R_{,\theta}R_{,z}R_{,\theta z}\right],\end{aligned} \tag{4}$$

where $\boldsymbol{\nabla}_s$ is the surface gradient operator, $R_{,\theta}=\partial R/\partial\theta$, $R_{,z}=\partial R/\partial z$, $R_{,\theta\theta}=\partial^2R/\partial\theta^2$, $R_{,zz}=\partial^2R/\partial z^2$, and $R_{,\theta z}=\partial^2R/(\partial\theta\partial z)$. A linearized expression for H is given below [see Eq. (24)].

B. Linear bulk and surface momentum balance equations

We consider the stability of a thin, initially axisymmetric, cylindrical nematic fiber surrounded by an inviscid matrix. The nematic liquid crystal is assumed to be incompressible, and its orientation is homogeneous and constant. Linear sta-

bility analysis is used to analyze the complete set of axisymmetric and nonaxisymmetric capillary instabilities in nematic liquid crystal fibers. Since the director is fixed, only the surface and bulk linear momentum balance equations define the evolution of the fiber's shape. In this work, the mechanical response of the nematic fluid is that of an anisotropic viscoelastic material [10,22], where the bulk is viscous and the surface is elastic.

The bulk linear momentum balance equation for this system is given by

$$\rho \frac{\partial \mathbf{v}}{\partial t} = \boldsymbol{\nabla} \cdot \mathbf{t}, \tag{5}$$

where ρ is the density, $\mathbf{v}$ the velocity vector, and $\mathbf{t}$ the total stress tensor. Inertia is neglected. The total stress tensor $\mathbf{t}$ is defined as

$$\mathbf{t} = -p\mathbf{I} + \mathbf{t}^{v}, \tag{6}$$

where p is the pressure, $\mathbf{I}$ the unit tensor, and $\mathbf{t}^{v}$ the viscous stress tensor. Although nematic liquid crystals have bulk Frank elasticity due to orientation gradients, in this paper no elastic stresses arise because $\mathbf{n}$ is held constant. Thus, the viscous stress tensor $\mathbf{t}^{v}$ is expressed by Ericksen's transversely isotropic fluid (TIF) constitutive equation [24]

$$\mathbf{t}^{v} = 2\eta_2 \mathbf{A} + \eta_3 \mathbf{A}:\mathbf{nnnn} + 2(\eta_1 - \eta_2)(\mathbf{A}\cdot\mathbf{nn} + \mathbf{nn}\cdot\mathbf{A}), \tag{7}$$

where η_1, η_2, and η_3 are viscosity coefficients, and $\mathbf{A}$ is the rate of deformation tensor given by

$$\mathbf{A} = \frac{1}{2}[\boldsymbol{\nabla}_{\mathbf{v}} + (\boldsymbol{\nabla}\mathbf{v})^{T}], \tag{8}$$

where the superscript ''T'' denotes the transpose. When $\eta_1 = \eta_2$ and $\eta_3 = 0$, the constitutive equation for Newtonian fluids is recovered. The TIF equation thus describes an anisotropic viscous material, whose viscosity depends on the director orientation. The continuity equation for this system is written as

$$\frac{\partial v_z}{\partial z} + \frac{1}{r}\frac{\partial (r v_r)}{\partial r} = 0. \tag{9}$$

In addition to the *bulk* linear momentum balance equation, the presence of an evolving free surface involves the action of surface forces, and thus the *surface* linear momentum balance equation enters the description. The surface linear momentum balance equation is given by [1,16]

$$\mathbf{N}\cdot\mathbf{t} = \boldsymbol{\nabla}_s \cdot \mathbf{t}^{\mathrm{SE}}, \tag{10}$$

where $\mathbf{t}^{\mathrm{SE}}$ is the surface elastic stress tensor. On the right hand side of Eq. (10), the surface viscous stresses are ignored since they are insignificant in relation to the surface elastic stresses. The shape of the evolving fiber depends only on the normal component of the surface linear momentum balance equation, and thus the shape equation is

$$\mathbf{N}\cdot\mathbf{t}\cdot\mathbf{N} = (\boldsymbol{\nabla}_s \cdot \mathbf{t}^{\mathrm{SE}})\cdot\mathbf{N}. \tag{11}$$

To make further progress, an expression for the surface elastic stress tensor $\mathbf{t}^{\mathrm{SE}}$ is required. Since nematic liquid crystals are anisotropic viscoelastic materials, anisotropy is an essential feature of $\mathbf{t}^{\mathrm{SE}}$. Moreover, surface elastic stresses are defined by constrained variations of the surface energy, which we now discuss.

The simplest expression for the surface free energy of the nematic liquid crystal is given by the Rapini-Papoular constitutive equation [16,22]

$$\gamma = \gamma_{\mathrm{is}} + \frac{\gamma_{\mathrm{an}}}{2}(\mathbf{n}\cdot\mathbf{N})^2 = \gamma_{\mathrm{is}}\left[1 + \frac{\tau}{2}(\mathbf{n}\cdot\mathbf{N})^2\right], \tag{12}$$

where γ_{is} is the isotropic surface tension, γ_{an} the anchoring energy due to the nematic orientation at the surface, and $\tau = \gamma_{\mathrm{an}}/\gamma_{\mathrm{is}}$ the ratio of the anchoring energy to isotropic surface tension. Since the surface free energy and the isotropic surface tension are always positive, τ is restricted to a value greater than -2. If $\tau = 0$, the surface anisotropy vanishes. For $\tau > 0$, the surface ''easy axis,'' that which minimizes the surface free energy, is parallel to the surface (planar anchoring) and perpendicular to the surface normal vector. For $\tau < 0$, the surface easy axis is perpendicular to the surface (homeotropic anchoring) and parallel to the surface normal vector. Extensions of the Rapini-Papoular constitutive equation are used in the literature, specifically to describe thermally induced surface orientation transitions [13], but these thermal effects are beyond the scope of this paper.

The expression for the surface elastic stress tensor $\mathbf{t}^{\mathrm{SE}}$ is obtained by considering the energetic penalty of constrained variations in γ and is given by the sum of the normal (tension) $\mathbf{t}_N^{\mathrm{SE}}$ and the bending $\mathbf{t}_B^{\mathrm{SE}}$ contributions [29]

$$\mathbf{t}_N^{\mathrm{SE}} = \gamma \mathbf{I}_s, \mathbf{t}_B^{\mathrm{SE}} = -\mathbf{I}_s \cdot \left(\frac{\partial \gamma}{\partial \mathbf{N}}\mathbf{N}\right). \tag{13}$$

Parametrizing the interface with orthonormal unit surface base vectors $(\mathbf{i}_1, \mathbf{i}_2)$, the normal and bending surface elastic stresses become

$$\mathbf{t}_N^{\mathrm{SE}} = \left[\gamma_{\mathrm{is}} + \frac{\gamma_{\mathrm{an}}}{2}(\mathbf{n}\cdot\mathbf{N})^2\right](\mathbf{i}_1\mathbf{i}_1 + \mathbf{i}_2\mathbf{i}_2), \tag{14a}$$

$$\mathbf{t}_B^{\mathrm{SE}} = B_{13}^{NI}\mathbf{i}_1\mathbf{N} + B_{23}^{N1}\mathbf{i}_2\mathbf{N}, \tag{14b}$$

where the superscript ''NI'' denotes the interface between the nematic liquid crystal (N) and isotropic fluid (I), which is inviscid in this study, and where the bending coefficients $\{B_{13}^{NI}, B_{23}^{NI}\}$ are given by

$$B_{13}^{NI} = -\gamma_{\mathrm{an}}(\mathbf{n}\cdot\mathbf{N})(\mathbf{n}\cdot\mathbf{i}_1), \quad B_{23}^{NI} = -\gamma_{\mathrm{an}}(\mathbf{n}\cdot\mathbf{N})(\mathbf{n}\cdot\mathbf{i}_2). \tag{15}$$

The bending coefficients are proportional to the anchoring energy and to the director's projections along the unit normal and along the surface base vectors. The largest magnitudes of the bending coefficients, for given γ_{an}, arise at $\pi/4$ angles

from the interface, and they vanish at the planar and homeotropic orientations. In matrix form, the 2×3 surface elastic stress tensor $\mathbf{t}^{\mathrm{SE}}$ is

$$\mathbf{t}^{\mathrm{SE}}=\begin{bmatrix}\gamma & 0 & B_{13}^{NI}\\ 0 & \gamma & B_{23}^{NI}\end{bmatrix}. \tag{16}$$

Clearly the surface stress tensor is asymmetric. Moreover, such bending stresses are intrinsic to nematic interfaces and result in forces normal to the interface, even in the absence of curvature, for a director field not parallel or perpendicular to the interface. The bending stresses play a crucial role in the capillary instability of nematic fibers. Isotropic surface tension leads to axisymmetric capillary instabilities, but anisotropic surface tension leads, through the generation of bending stresses, to nonaxisymmetric modes. The reason behind this statement is that forces normal to the interface depend on surface orientation and exist even in the absence of curvature [20,29].

Using the expression for the surface elastic stress tensor $\mathbf{t}^{\mathrm{SE}}$, we find the following expression for the interfacial force $\mathbf{f}$ [29]:

$$\mathbf{f}=\boldsymbol{\nabla}_s\cdot\mathbf{t}^{\mathrm{SE}}=\boldsymbol{\nabla}_s\cdot\mathbf{t}_N^{\mathrm{SE}}+\boldsymbol{\nabla}_s\cdot\mathbf{t}_B^{\mathrm{SE}}=\left\{\left[\left(\frac{\partial\gamma}{\partial\mathbf{n}}\right)\cdot(\boldsymbol{\nabla}_s\mathbf{n})^T\right]\cdot\mathbf{I}_s+(2H\gamma)\mathbf{N}\right\}+\left\{\left[-2H\left(\frac{\partial\gamma}{\partial\mathbf{N}}\cdot\mathbf{N}\right)-\nabla_s\cdot\left(\frac{\partial\gamma}{\partial\mathbf{N}}\right)\right]\mathbf{N}\right\}, \tag{17}$$

where the first term in curly brackets is the normal stress contribution and the second term in curly brackets is the bending stress contribution. Equation (17) shows that surface gradients in the normal (tension) surface stress $\mathbf{t}_N^{\mathrm{SE}}$ give rise to tangential (perpendicular to $\mathbf{N}$) and normal forces (parallel to $\mathbf{N}$), while surface gradients of bending stress $\mathbf{t}_B^{\mathrm{SE}}$ give rise only to normal forces. It is shown in Eq. (17) that normal forces from surface gradients of bending stress persist even in the absence of curvature ($H=0$). Meanwhile, tangential forces have been shown to drive Marangoni nematic flows [29].

The normal component of Eq. (17) is known as the generalized Laplace equation [1]

$$-\mathbf{N}\cdot(\mathbf{t}^I-\mathbf{t}^N)\cdot\mathbf{N}=(\boldsymbol{\nabla}_s\cdot\mathbf{t}^{\mathrm{SE}})\cdot\mathbf{N}=-p_\gamma, \tag{18}$$

where the superscript ''I'' and ''N'' denote the isotropic and nematic fluids, respectively, and p_γ is the magnitude of the interfacial normal force originating from the surface gradients of the normal and bending stresses, called as the capillary pressure, and according to Eq. (17) it is given by

$$-p_\gamma=2H\gamma-2H\left(\frac{\partial\gamma}{\partial\mathbf{N}}\cdot\mathbf{N}\right)-\boldsymbol{\nabla}_s\cdot\left(\frac{\partial\gamma}{\partial\mathbf{N}}\right). \tag{19}$$

Thus, the normal and bending stress contributions to the capillary forces are

$$p_\gamma|_{\text{normal stresses}}=-2H\gamma, \tag{20}$$

$$p_\gamma|_{\text{bending stresses}}=2H\left(\frac{\partial\gamma}{\partial\mathbf{N}}\cdot\mathbf{N}\right)+\boldsymbol{\nabla}_s\cdot\left(\frac{\partial\gamma}{\partial\mathbf{N}}\right). \tag{21}$$

Thus, the anchoring energy γ_{an} contributes to the capillary pressure through both the *normal* and *bending* stresses. Nevertheless, when considering the linear regime of capillary instability of a nematic liquid crystal fiber, second order terms involving $H(\mathbf{n}\cdot\mathbf{N})^2$ cancel out and the only remaining anisotropic contribution to the capillary pressure is that from the bending stresses. Thus, any model that attempts to capture the linear regime of capillary instability in a nematic liquid crystal fiber must include all contributions arising from the bending stress tensor.

C. Simplifying assumptions

The assumptions made to describe the linear regime of the capillary instability in incompressible, isothermal nematic fibers are as follows.

(a) For sufficiently thin fibers, the surface elastic energy is insignificant with respect to the bulk Frank elasticity [22]; the director field does not change even if the fiber shape evolves through the linear instability process.

(b) In the long wavelength approximation, the wavelength of a dominant surface disturbance is assumed to be much longer than the fiber radius, and the axial velocity is considerably larger than the other velocity components. In the present case, an order of magnitude calculation obtained using the continuity equation yields $v_z\gg v_r,v_\theta$ [2]. Thus, only the axial velocity v_z is significant.

(c) In the absence of surrounding matrix effects and in the long wavelength approximation, the radial dependence of axial velocity is ignored so that the axial velocity is considered as a function only of the axial coordinate and time $v_z(z,t)$ [2].

(d) The analysis is restricted to the linear regime of the capillary instability. This restriction is obeyed when $\xi/a\ll1$.

In the next section, we develop the governing equations for the capillary instabilities of nematic fibers when the director is aligned along the fiber axis ($n_z=1$).

D. Governing equations for an axial nematic fiber

In this section, the governing equation of the surface disturbance $\xi(z,\theta,t)$, Eq. (3), is derived for the axial fiber by combining the linear momentum balance equation, Eq. (5), and the normal stress boundary condition Eq. (18).

During nonaxisymmetric capillary instability, the principal radii of the curvature $(R_{r\theta},R_{rz})$ and the unit surface normal vector $\mathbf{N}$ are obtained in the linear regime using the assumptions in Sec. II C and given by

$$\frac{1}{R_{r\theta}}=\frac{1}{R}-\frac{1}{R^2}\left(\frac{\partial^2R}{\partial\theta^2}\right),\quad\frac{1}{R_{rz}}=-\frac{\partial^2R}{\partial z^2}, \tag{22}$$

$$\mathbf{N}=\mathbf{i}_r-\frac{1}{R}\frac{\partial R}{\partial\theta}\mathbf{i}_\theta-\frac{\partial\mathbf{R}}{\partial z}\mathbf{i}_z. \tag{23}$$

Note that the radii of curvature are θ dependent: $R_{r\theta}=R_{r\theta}(z,\theta,t)$, $R_{rz}=R_{rz}(z,\theta,t)$. Thus, the mean curvature H in Eq. (4) is expressed as [21]

$$H=-\frac{1}{2}\left(\frac{1}{R_{r\theta}}+\frac{1}{R_{rz}}\right)=-\frac{1}{2}\left[\frac{1}{R}-\frac{1}{R^2}\left(\frac{\partial^2 R}{\partial\theta^2}\right)-\frac{\partial^2 R}{\partial z^2}\right]. \tag{24}$$

Under the assumed kinematical conditions, the only nonzero component of **A** is

$$\mathbf{A}_{zz}=\frac{\partial v_z}{\partial z}. \tag{25}$$

The viscous stress tensor, obtained by substituting Eqs. (1) and (25) into Eq. (7), is

$$t^{v}_{zz}=2\eta\frac{\partial v_z}{\partial z}, \tag{26}$$

where $\eta=\eta_2+\eta_3/2+2(\eta_1-\eta_2)$. Substituting Eq. (26) into Eq. (6), the total stress tensor becomes

$$t_{zz}=-p+2\eta\frac{\partial v_z}{\partial z}. \tag{27}$$

Using Eqs. (23) and (24) in Eq. (19), the capillary pressure p_γ becomes

$$p_\gamma=\frac{\gamma_{is}}{a}-\frac{\gamma_{is}}{a^2}\xi-\gamma_{is}\left(\frac{\partial^2\xi}{\partial z^2}+\frac{1}{a^2}\frac{\partial^2\xi}{\partial\theta^2}\right)-\gamma_{is}\tau\frac{\partial^2\xi}{\partial z^2}, \tag{28}$$

which properly reduces to the Newtonian capillary pressure when $\tau=0$, i.e., when surface tension is isotropic. Importantly, when the bending stress contributes to the capillary pressure of an axial fiber, a force $p_\gamma|_{bf}$ appears that is given by

$$p_\gamma|_{bf}=-\gamma_{is}\tau\frac{\partial^2\xi}{\partial z^2}, \tag{29}$$

which can compete or cooperate with the usual isotropic contribution since the sign of τ is not fixed. Thus, τ in Eq. (28) can be positive, negative, or zero.

The pressure in Eq. (27) can be expressed in terms of the capillary pressure [2]

$$p=-\frac{1}{3}(t_{zz}+t_{\theta\theta}+t_{rr})=-\frac{1}{3}(t_{zz}-2p_\gamma), \tag{30}$$

where the following boundary conditions are applied: $t_{rr}=-p_\gamma$, $t_{\theta\theta}=t_{rr}$, at $r=a$.
Substituting Eq. (30) into Eq. (27), the total stress tensor is rewritten as [2]

$$t_{zz}=-p_\gamma+3\eta\frac{\partial v_z}{\partial z}. \tag{31}$$

Using Eq. (31), the axial momentum balance equation, Eq. (5), is found to be [2]

$$\rho\frac{\partial v_z}{\partial t}=-\frac{\partial p_\gamma}{\partial z}+3\eta\frac{\partial^2 v_z}{\partial z^2}. \tag{32}$$

By integrating the continuity equation, Eq. (9), across the cross section of the fiber, we obtain

$$\frac{\partial R}{\partial t}+v_z\frac{\partial R}{\partial z}+\frac{R}{2}\frac{\partial v_z}{\partial z}=0, \tag{33}$$

where the second term is dropped in the linear regime [2,31]. Thus, using Eq. (2) the axial velocity can be expressed in terms of ξ [2,31]:

$$\frac{\partial v_z}{\partial z}=-\frac{2}{a}\frac{\partial\xi}{\partial t}. \tag{34}$$

Combining Eqs. (32) and (34) in conjunction with Eq. (28) gives the differential equation for ξ:

$$\frac{\partial^2\xi}{\partial t^2}-\frac{3\eta}{\rho}\frac{\partial^3\xi}{\partial z^2\partial t}+\frac{\gamma_{is}a}{2\rho}\frac{\partial^2}{\partial z^2}\left[\frac{\xi}{a^2}+\left(\frac{\partial^2\xi}{\partial z^2}+\frac{1}{a^2}\frac{\partial^2\xi}{\partial\theta^2}\right)+\tau\frac{\partial^2\xi}{\partial z^2}\right]=0. \tag{35}$$

By substituting Eq. (3) into Eq. (35), a quadratic equation for the dimensionless growth rate $\alpha^*=\alpha\sqrt{\rho a^3/\gamma_{is}}$, is obtained:

$$\alpha^{*2}+3\mathrm{Oh}(ka)^2\alpha^*-\frac{(ka)^2}{2}[1-m^2-(1+\tau)(ka)^2]=0, \tag{36}$$

where ka is the dimensionless wave number and $\mathrm{Oh}=\eta/\sqrt{\rho\alpha\gamma_{is}}$ is the Ohnesorge number, or the ratio of the viscous force to the surface force. From Eq. (36), the nematic fibers are unstable when the condition is satisfied:

$$2\alpha^*=-3\,\mathrm{Oh}(ka)^2+\sqrt{[3\mathrm{Oh}(ka)^2]^2+2(ka)^2[1-m^2-(1+\tau)(ka)^2]}>0. \tag{37}$$

The maximum growth rate $\alpha^*_{\max}$ and the corresponding wave number $ka_{\max}$, obtained by solving Eq. (36), are

$$\alpha^*_{\max}=\left(2\sqrt{2}\sqrt{\frac{(1+\tau)}{(1-m^2)^2}}+\frac{6\mathrm{Oh}}{(1-m^2)}\right)^{-1}, \tag{38}$$

$$ka_{\max}=\left(\sqrt{\frac{2(1+\tau)}{(1-m^2)}}+3\sqrt{2}\mathrm{Oh}\sqrt{\frac{(1+\tau)}{(1-m^2)^2}}\right)^{-1}, \tag{39}$$

which reduce to the results for Newtonian fluids if the viscoelastic anisotropy and the nonaxisymmetric dependence vanish; i.e., $\eta_1=\eta_2$, $\eta_3=0$, $\tau=0$, and $m=0$: for the highly viscous fiber, $\alpha^*_{\max}=1/(6\mathrm{Oh})$ and $ka_{\max}=1/\sqrt{3\sqrt{2}\mathrm{Oh}}$; for the inviscid fiber, $\alpha^*_{\max}=1/2\sqrt{2}$ and $ka_{\max}=1/\sqrt{2}$. In particular, when only axisymmetric disturbances become unstable, i.e., $m=0$, the results from Eqs. (38) and (39) predict the axial fiber breakup into droplets with a characteristic size of $2\pi/ka_{\max}$ [25].

The physics of capillary instabilities in axial nematic fibers can be elucidated by rewriting Eq. (28) as

$$p_\gamma=\frac{\gamma_{is}}{a}-\frac{\gamma_{is}}{a^2}\xi-\gamma_{is}\left(\frac{\partial^2\xi}{\partial z^2}+\frac{1}{a^2}\frac{\partial^2\xi}{\partial\theta^2}\right)-\gamma_{is}\tau\frac{\partial^2\xi}{\partial z^2}=\frac{\gamma_{is}}{a}+f_d+f_c, \tag{40}$$

$$f_d=-\frac{1}{a^2}C_\xi\xi,\quad f_c=-\frac{1}{a^2}C_{\xi_{\theta\theta}}\xi_{\theta\theta}-C_{\xi_{zz}}\xi_{zz},$$

$$C_\xi=C_{\xi_{\theta\theta}}=\gamma_{is},\quad C_{\xi_{zz}}=\gamma_{is}(1+\tau). \tag{41}$$

The capillary pressure contains two (ξ-dependent) deformation effects: a displacement force f_d and a curvature force f_c. Capillary instabilities occur because a spatially periodic pressure gradient develops, inducing macroscopic flow. The driving force for creating a pressure gradient is denoted as a destabilizing force, while a force resisting it is denoted as a stabilizing force. The nature of the two capillary forces depends only on the sign of their coefficients C_ξ, $C_{\theta\theta}$, and $C_{\xi_{zz}}$, which are the effective surface tensions for both forces. Thus the displacement force is destabilizing (stabilizing) for $C_\xi>0$ ($C_\xi<0$), while the curvature force is stabilizing (destabilizing) for $C_{\theta\theta}>0$ and $C_{\xi_{zz}}>0$ ($C_{\theta\theta}<0$ and $C_{\xi_{zz}}<0$). In isotropic fibers ($\tau=0$), the displacement force is always destabilizing and the curvature force is always stabilizing, thus explaining the existence of lower cutoff in the instability wavelength, as in the classical Rayleigh fiber instability (see Fig. 3 and discussion below). This occurs because the stabilizing curvature force for sufficiently short wavelengths overpowers the driving displacement force. Since for axial fibers $C_\xi>0$, the displacement force is always destabilizing. On the other hand, since $\tau\geqslant-2$, the curvature force from ξ_{zz} can be destabilizing if $\tau<-1$ because $C_{\xi_{zz}}<0$ or stabilizing if $\tau>-1$ because $C_{\xi_{zz}}>0$, although the curvature force from $\xi_{\theta\theta}$ is always stabilizing. Thus, when the curvature force from ξ_{zz} is destabilizing ($\tau<-1$), a lower cutoff wavelength does not exist and the instability must be of the Hadamard type (see Fig. 2 and discussion below). Since τ is the bending force coefficient [see Eq. (29)], the described phenomenology of capillary instabilities in axial fibers is attributed to anisotropic effects arising from surface gradients of bending stresses.

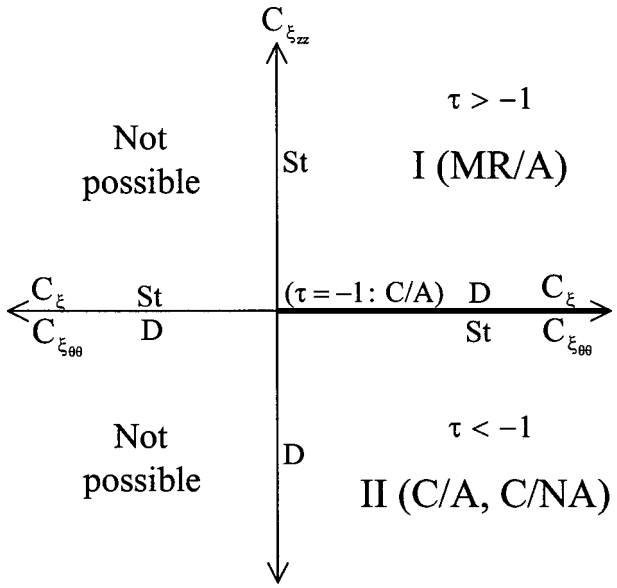

FIG. 2. Instability phase diagram in terms of the displacement force coefficient C_ξ and the curvature force coefficients $C_{\xi_{\theta\theta}}$ and $C_{\xi_{zz}}$. Roman numerals (I, II) refer to the two regions of Table I, and the captions (MR/A, C/A, C/NA) to the instability types of Table I. On the axes St and D denote stabilizing and destabilizing, respectively.

III. RESULTS AND DISCUSSION

The characterization of capillary instabilities in nematic fibers requires the specification of two features: (i) Instability mechanism and (ii) Symmetry of deformation modes. These two features are embedded in Eq. (37) and must be considered separately.

(i) Instability mechanism. The capillary instabilities in nematic liquid crystalline fibers are found to follow two different routes: Modified Rayleigh and catastrophic instability mechanisms.

(a) Modified Rayleigh (MR) instability mechanism. The modified Rayleigh instability is characterized by a single $m=0$ mode. Setting $m=0$ in Eqs. (37)–(39), we find that the nematic fibers are MR unstable whenever

$$2\alpha^*(m=0)=-3\mathrm{Oh}(ka)^2+\sqrt{[3\mathrm{Oh}(ka)^2]^2+2(ka)^2[1-(1+\tau)(ka)^2]}>0,$$
$$\alpha^*_{\max}(m=0)=(2\sqrt{2}\sqrt{(1+\tau)}+6\mathrm{Oh})^{-1}>0,\quad 0<k\alpha_{\max}(m=0)=(\sqrt{2(1+\tau)+3\sqrt{2}\mathrm{Oh}\sqrt{(1+\tau)}})^{-1}<ka_{\mathrm{cutoff}}, \tag{42}$$

where ka_{cutoff} is an upper cutoff wave number above which disturbances do not grow. The axial fibers have no azimuthal dependence and thus axisymmetric.

(b) Catastrophic simultaneous instability mechanism. In the catastrophic simultaneous instability mechanism, unstable modes follow the classical short wave (small wavelength) instability [30], which is characterized by simultaneous occurrence of all azimuthal modes m with unbounded growth rate. Using Eq. (37), we find that the nematic fibers are catastrophic unstable whenever

$$2\alpha^* = -3\mathrm{Oh}(ka)^2 + \sqrt{[3\mathrm{Oh}(ka)^2]^2 + 2(ka)^2[1-m^2-(1+\tau)(ka)^2]} > 0, \quad \frac{d\alpha^*}{d(ka)} > 0, \tag{43}$$

where $ka>0$ for a catastrophic instability without upper ka_{cutoff}. Under this instability mechanism, the following ordering in growth rates is found:

$$\alpha^{*0} > \alpha^{*1} > \cdots > \alpha^{*n} > \alpha^{*n+1} > \cdots, \tag{44}$$

where $\alpha^*(m_n) \equiv \alpha^{*n}$ while m_n represents $m=n$ mode hereafter.

(ii) Symmetry of deformation modes. The symmetry of the deformation in this paper is restricted to axisymmetric and nonaxisymmetric modes, axisymmetric modes being rotationally invariant. It is noted that for axial fibers the mode $m=0$ is, as usual, an axisymmetric mode.

Based on this general discussion, the criteria required to classify the capillary instability are given by specification of instability mechanism/symmetry. The following three cases emerge: (a) Modified Rayleigh/axisymmetric (MR/A), (b) catastrophic/axisymmetric (C/A), (c) catastrophic/nonaxisymmetric (C/NA). In what follows we discuss these three different capillary instabilities in axial fibers, and determine the parametric dependence of the deformation and growth rates.

A. Capillary instabilities in axial fibers

Table I summarizes the complete phenomenology of the three capillary instabilities in axial fibers, as computed from Eqs. (42), (43). There are three regimes according to the values of τ. The first column shows the instability type, and the entries show characteristic growth rate curves for each instability mechanism. For the MR instability in the second column, the growth rate curve is bounded, and an upper ka_{cutoff} exists. For the catastrophic instabilities of all modes in the fourth column, the growth rate curves are unbounded, and lower modes grow faster than higher modes. We next discuss in detail the physical and mathematical aspects of the tabulated information.

1. Instability characterization in axial fibers

As explained above the physics of capillary instabilities in axial fibers, as summarized in Table I, is elucidated by considering the sign of the displacement and curvature force coefficients or effective surface tensions [see Eqs. (41c), (41d)]. Figure 2 presents an instability phase diagram spanned by the displacement force coefficient C_ξ, and the curvature force coefficients $C_{\xi_{\theta\theta}}$ and $C_{\xi_{zz}}$. The roman numerals (I, II) refer to the two regions of Table I, and the captions (MR/A, C/A, C/NA) to the instability types of Table I. The figure captures the nature of the driving forces and identifies when and why an instability occurs. For the axial fiber, since $C_\xi(C_{\xi\theta\theta})$ is always positive and thus destabilizing (stabilizing), the sign of $C_{\xi_{zz}}$ determines instability mechanisms: The first quadrant corresponds to instabilities with an upper ka_{cutoff} since the curvature forces are stabilizing; in the fourth quadrant, curvature from ξ_{zz} destabilizes and catastrophic instabilities occur; the second and third quadrants are thermodynamically inaccessible since C_ξ and $C_{\xi_{\theta\theta}}$ are always positive. By crossing the boundary between the first and fourth quadrants ($\tau=-1$), the fiber under MR instability in region I becomes susceptible to catastrophic instability for mode $m=0$. And then, in region II the fiber is catastrophic, unstable for modes $m\geqslant 1$ as well as $m=0$. Figure 3 shows a representative schematic of the displacement (f_d) and curvature ($f_{c,\xi_{zz}}, f^{m0}_{c,\xi_{\theta\theta}}, f^{m}_{c,\xi_{\theta\theta}}$) forces as a function of the dimensionless anchoring energy τ, where $f_{c,\xi_{zz}}$ represents the curvature forces from ξ_{zz}, $f^{m0}_{c,\xi_{\theta\theta}}$ the curvature force from $\xi_{\theta\theta}$ for $m=0$ mode, and $f^{m}_{c,\xi_{\theta\theta}}$ for $m\geqslant 1$ modes. The figure again provides the reasons of the existence of the two regions (I and II), and observation of the sign and relative magnitudes of the stabilizing and destabilizing forces explains the phenomenology of Table I. In short, the displacement forces (f_d) are always destabilizing, while the curvature forces from $\xi_{\theta\theta}$ ($f^{m0}_{c,\xi_{\theta\theta}}, f^{m}_{c,\xi_{\theta\theta}}$) always stabilizing, showing the smaller curvature force for $m=0$ than for $m\geqslant 1$. Meanwhile, the curvature forces from $\xi_{zz}(f_{c,\xi_{zz}})$ are stabilizing only for $\tau>-1$. In Fig. 3, the stabilizing forces for the nonaxisymmetric modes ($f^{m}_{c,\xi_{\theta\theta}}$) are sufficiently strong to quench the instability if $\tau>-1$, and thus only $m=0$ is unstable. In other words, it is energetically costly to cause instability modes $m\geqslant 1$ for $\tau>-1$ as seen by comparing the magnitude of stabilizing forces with that of destabilizing forces. For $\tau=-1$, since the destabilizing f_d cannot overcome the stabiliz-

TABLE I. Capillary instabilities in axial fibers. MR/A: Modified Rayleigh/axisymmetric instability. C/A: Catastrophic/axisymmetric instability. C/NA: Catastrophic/nonaxisymmetric instability. α^{*i}: Growth rate of ith mode for catastrophic instabilities.

Instability type	Region I ($\tau>-1$)	Criticality ($\tau=-1$)	Region II ($-1>\tau\geq-2$)
MR/A	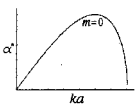	No	No
C/A	No	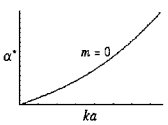	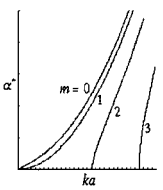 $(\alpha^{*0}>\alpha^{*1}>\alpha^{*2}>\cdots)$
C/NA	No	No	

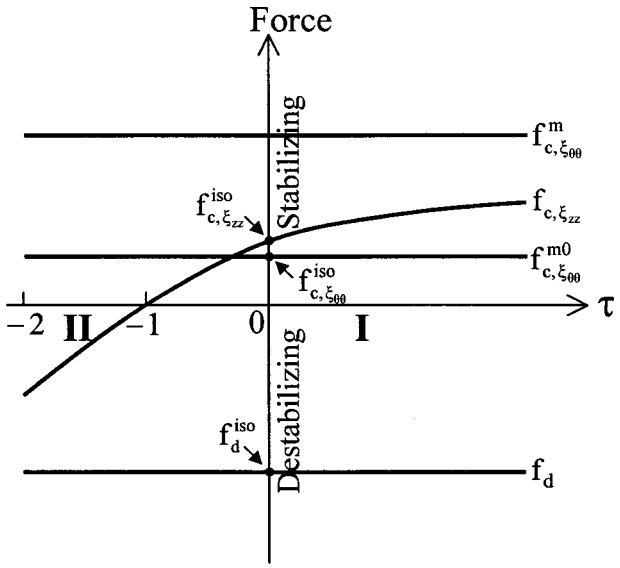

FIG. 3. Representative schematic of the displacement (f_d) and curvature ($f_{c,\xi_{zz}}, f^{m0}_{c,\xi_{\theta\theta}}, f^{m}_{c,\xi_{\theta\theta}}$) forces as a function of the dimensionless anchoring energy τ, where $f_{c,\xi_{zz}}$ represents the curvature forces from ξ_{zz}, $f^{m0}_{c,\xi_{\theta\theta}}$ the curvature force from $\xi_{\theta\theta}$ for $m=0$ mode, and $f^{m}_{c,\xi_{\theta\theta}}$ for $m\geqslant 1$ modes. In the figure, $f^{\rm iso}_{d}$ represents the displacement force, and $f^{\rm iso}_{c,\xi_{\theta\theta}}$ and $f^{\rm iso}_{c,\xi_{zz}}$ the curvature forces for isotropic fibers. The figure provides the reasons of the existence of the two regions (I and II), and observation of the relative magnitudes of the stabilizing and destabilizing forces explains the phenomenology of Table I.

ing $f^{m}_{c,\xi_{\theta\theta}}$ and $f_{c,\xi_{zz}}$ is no longer stabilizing, only $m=0$ undergoes catastrophic instability. The figure also shows that for isotropic fibers ($\tau=0$) the curvature forces $f^{\rm iso}_{c,\xi_{\theta\theta}}$ and $f^{\rm iso}_{c,\xi_{zz}}$ are always stabilizing while the displacement force $f^{\rm iso}_{d}$ is always destabilizing, and thus the upper $ka_{\rm cutoff}$ exists since the magnitude of the destabilizing force is relatively greater than that of the total stabilizing curvature forces.

The nature of nonaxisymmetric instabilities is explained as follows. For the cylindrical axial fiber, the surface orientation of the nematic texture is planar anchoring. Since for $\tau>0$ the easy axis of the surface is planar anchoring, the misalignment between the surface orientation and the easy axis is not high enough to cause the nonaxisymmetric instability by bending stresses. On the other hand, for $\tau<0$ the misalignment between the actual director and the easy axis (homeotropic) is large, and if the anchoring energy (τ) is strong enough (large negative value), the bending stresses may even cause nonaxisymmetric deformation in order to relieve the high misalignment and align the director with the easy axis by means of surface deformations and rotations. These observations on the symmetry of the unstable modes can be made quantitative, as follows. When the growth rate α^* is real and positive, the surface disturbances become unstable and grow with time. In the Newtonian fiber ($\tau=0$) the positive real α^* is obtained only for the axisymmetric disturbances ($m=0$), from Eq. (37). For the axial fiber, by solving Eq. (37) positive real α^* solutions are obtained when the following condition is satisfied:

$$1-m^2-(1+\tau)(k\alpha)^2>0. \tag{45}$$

For isotropic fibers, $\tau=0$ and inequality Eq. (45) is never fulfilled for $m\geqslant 1$, but for nematic fibers it can be. Inequality Eq. (45) is satisfied when $\tau<-1$, where the following condition is also satisfied:

$$0<\frac{1-m^2}{1+\tau}<(ka)^2. \tag{46}$$

In other words, when the magnitude of the stabilizing curvature force $f_{c,\xi_{zz}}$ is sufficiently reduced by bending forces, and eventually $f_{c,\xi_{zz}}$ becomes destabilizing because the effective surface tension is negative, nonaxisymmetric modes emerge under catastrophic Hadamard instabilities. Since curvature from ξ_{zz} is destabilizing, there is no upper cutoff but lower cutoff wave number for $m\geqslant 2$ from Eq. (46).

For axial fibers we then have two instability regions.

(a) MR/A: $\tau<-1$, region I. This case corresponds to the second column of Table I. When $\tau>-1$ only the modified Rayleigh instability with a single unstable m_0 mode is present. The mode is axisymmetric. In this case, the effective surface tensions are positive and the instability follows the classical Rayleigh mode.

(b) C/NA and C/A: $-2\leqslant\tau<-1$, region II. This case corresponds to the fourth column of Table I. There are two possible instabilities: C/NA and C/A. The catastrophic instability mechanism controls the fiber: All modes are unstable, and the short wave instability is dominant. The lower modes grow faster than the higher modes at constant τ, which means lower mode disturbances with short wavelengths are more likely to cause the fiber instability. In this regime destabilizing forces dominate, and the negative effective surface tension of curvature force $f_{c,\xi_{zz}}$ allows for surface fibrillation.

(c) Criticality: $\tau=-1$. The third column in Table I shows that when $\tau=-1$ there is a critical state involving C/A instability. In the limit $\tau=-1^{+}$ the growth rate of the MR/A instability becomes maximized. On the other hand, in the limit $\tau=-1^{-}$ the C/A and C/NA instabilities shrink to the only C/A instability with a smaller slope of growth rate. Thus, decreasing τ through the value of -1 denotes the extinction of the bounded MR instability, and the birth of the unbounded catastrophic instabilities.

2. Symmetry of deformation modes in axial fibers

In this study, surface disturbances are classified by the mode m in the azimuthal direction given in Eq. (3). Because m is an integer, positive and negative signs are equally possible for each value of m. In axial fibers, the sign selects the handedness of the shape deformation but does not affect the growth rate curves due to the m^2 dependence of the growth rate in Eq. (37). A positive sign imprints a left-handed rotation to the surface pattern and thus these are chiral modes. The mode m_0, which is a so-called varicose mode, represents the well-known axisymmetric disturbance. Likewise, the m_1 mode is called the sinuous mode, and modes with $m\geqslant 2$, fluted modes. Under the mode m_1 instability, the cen-

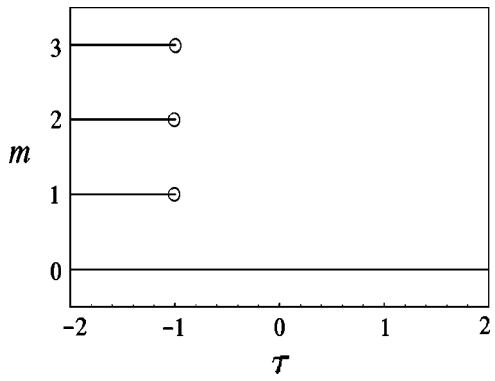

FIG. 4. Azimuthal wave number m as a function of the dimensionless anchoring energy τ. At $\tau=-1$, the figure shows the transition of instability mechanisms from MR to catastrophic type. Only the m_0 mode is unstable in the whole range of τ. The instability birth curve diverges as $\tau\rightarrow-1^+$, and thus the m_0 mode undergoes from MR for $\tau>-1$ to catastrophic for $\tau\leqslant-1$. Nonaxisymmetric catastrophic instabilities also emerge when $\tau<-1$.

ter of the fiber moves along a spiral trajectory around the z axis. For $m\geqslant 2$, the cross-sectional shape has a regular pattern identified by m axes of rotational symmetry, and the shape rotates along the z axis. The axial rotation of the anisotropic cross-sectional shape for $m\geqslant 2$, produces twisted ridged microstructures.

It is noted that while values Oh>0 change the maximum growth rate and the corresponding wave number, they have no effect on the surface deformation pattern. For the classical m_0 mode, $\lambda=2\pi/(ka)$ is the dimensionless wavelength of the varicose shape in the z direction. The fiber cross section is always circular but periodically expands and contracts when traversing the axial fiber direction. Thus, for the m_0 mode the formation of droplets with a characteristic size λ is predicted.

3. Parametric effects on capillary instabilities in axial fibers

Figure 4 shows the azimuthal wavenumber m as a function of the dimensionless surface anchoring energy τ. At $\tau=-1$, the figure shows the transition of instability mechanisms from MR to catastrophic type. Only the MR mode m_0 persists for $\tau>-1$ because the stabilizing curvature forces $f^m_{c,\xi_{\theta\theta}}$ for modes $m\geqslant 1$ are sufficiently strong, while if $\tau<-1$ all catastrophic modes arise simultaneously since curvature forces $f_{c,\xi_{zz}}$ are destabilizing and thus total destabilizing forces are greater than total stabilizing forces for all modes (see Fig. 3). The instability birth curve diverges as $\tau\rightarrow-1^+$, indicating that in this $\tau=-1$ limit, the m_0 mode becomes catastrophic unstable.

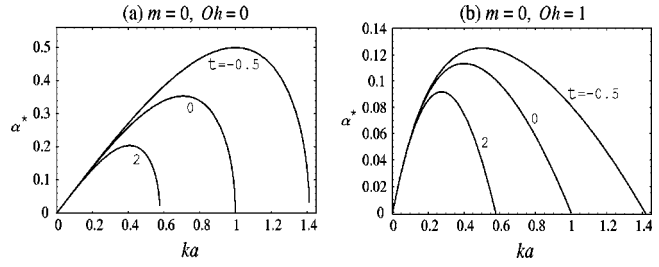

FIG. 5. Dimensionless growth rate curves α^* as a function of dimensionless wavenumber ka, for m_0 at $\tau=-0.5,0,2$, for (a) Oh $=0$ and (b) Oh$=1$. This figure corresponds to region I in Table I, and the only m_0 mode is MR unstable.

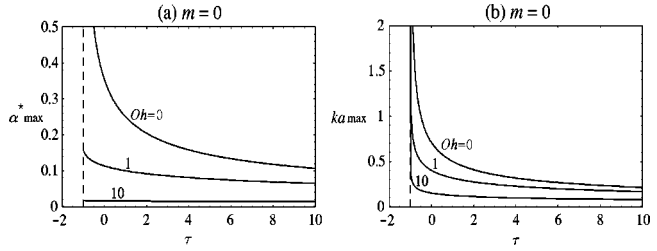

FIG. 6. (a) Maximum growth rate $\alpha^*_{\max}$ and (b) corresponding maximum dimensionless wave number $ka_{\max}$ as a function of dimensionless anchoring energy τ, for m_0 and Oh$=0,1,10$. This figure corresponds to region I in Table I and to the MR/A instability.

Figure 5 shows the dimensionless growth rate curves α^* as a function of dimensionless wave number ka, for m_0 at $\tau=-0.5,0,2$, for (a) Oh$=0$ and (b) Oh$=1$. This figure corresponds to region I in Table I. According to Eq. (42), at three values of τ, $\tau=-0.5$, 0, and 2, the only unstable mode is m_0. It is seen in Fig. 5 that the cutoff wave number, which is given as $ka_{\text{cutoff}}=1/\sqrt{1+\tau}$, is not a function of Oh. In addition to decreasing the maximum growth rate, the effect of increasing Oh is to shift horizontally the maximum growth rate to lower ka values, meaning that viscosity increases the length scales of the unstable mode.

Figure 6(a) shows the maximum growth rate $\alpha^*_{\max}$, and Fig. 6(b) the corresponding maximum dimensionless wavenumber $ka_{\max}$ as a function of dimensionless anchoring energy τ, for m_0 and Oh$=0,1,10$. This figure corresponds to region I in Table I, and to the MR/A instability. The suppressing effect of the viscosity is again evident in both figures. The figure shows that as τ increases $\alpha^*_{\max}$ and $ka_{\max}$ decrease sharply until $\tau=0$, and then they decrease at a much slower rate. The sensitivity of the instability with respect to τ has already been explained in the previous section

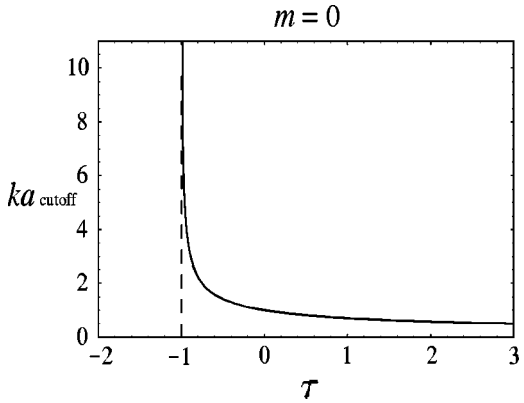

FIG. 7. Dimensionless cutoff wave number ka_{cutoff} as a function of the dimensionless anchoring energy τ, for m_0. This figure corresponds to region I in Table I, and to the MR/A instability.

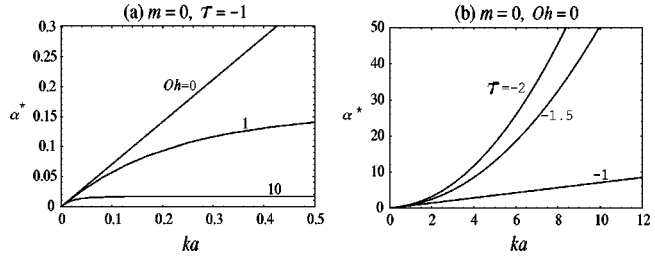

FIG. 8. Dimensionless growth rate curves α^* as a function of dimensionless wave number ka, for m_0, and (a) Oh$=0,1,10$, and $\tau=-1$, and (b) $\tau=-2,-1.5,-1$, and Oh$=0$. (a) Corresponds to the transition (C/A instability) between regions I and II, and (b) to the transition and region II in Table I.

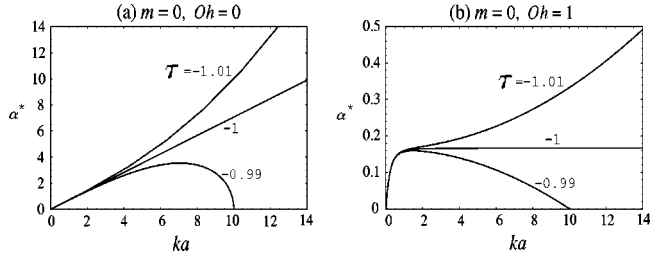

FIG. 9. Dimensionless growth rate curves α^* as a function of dimensionless wave number ka, for m_0 at $\tau=-0.99$, -1, and -1.01, and (a) Oh$=0$ and (b) Oh$=1$, dramatically revealing the critical point at $\tau=-1$. The dimensionless anisotropic elasticity values are close to $\tau=-1$ (transition between regions I and II in Table I), when controlled by the MR ($\tau=-0.99$; region I in Table I) and catastrophic ($\tau=-1.01$; region II in Table I) instability mechanisms, respectively.

in terms of the misalignment between the surface orientation and the easy axis.

Figure 7 shows the dimensionless cutoff wave number ka_{cutoff} as a function of the dimensionless anchoring energy, τ, for m_0. This figure corresponds to region I in Table I, and to the MR/A instability. The ka_{cutoff} decreases with τ in the same pattern as $ka_{\max}$ in Fig. 6(b). Similar to the viscous effect, if $\tau>-1$, the surface elasticity τ tends to stabilize the fiber, as explained above.

Figure 8 shows the dimensionless growth rate curves α^* as a function of dimensionless wave number ka, for m_0, and (a) Oh$=0,1,10$, and $\tau=-1$, and (b) $\tau=-2,-1.5,-1$, and Oh$=0$. Figure 8(a) corresponds to the transition (C/A instability) between regions I and II in Table I. According to Eq. (43), for $\tau=-1$ the only unstable mode is m_0, and the growth rate increases with wave number ka without ka_{cutoff}, signaling that axisymmetric catastrophic instability occurs but increasing Oh suppresses the slope of growth rate by means of the stabilization effect of viscosity. Figure 8(b) corresponds to the transition and region II in Table I. According to Eq. (43), as τ decreases from $\tau=-1$, the growth rate of mode m_0 increases faster with wave number ka under the catastrophic instability.

Figure 9 shows the dimensionless growth rate curves α^* as a function of dimensionless wave number ka, for m_0 at $\tau=-0.99$, -1, and -1.01, and (a) Oh$=0$, and (b) Oh$=1$, dramatically revealing the critical point at $\tau=-1$. The dimensionless anisotropic elasticity values are close to $\tau=-1$ (transition between regions I and II in Table I), when controlled by the MR ($\tau=-0.99$; region I in Table I) and catastrophic ($\tau=-1.01$; region II in Table I) instability mechanisms, respectively. The growth rate curves are bounded at ka_{cutoff} for $\tau=-0.99$ while the short wave instabilities are seen for $\tau=-1$ and -1.01. Although, considering that the MR instability is maximized as $\tau\rightarrow-1^+$ while the catastrophic instability is minimized as $\tau\rightarrow-1^-$, the latter is always more unstable in the whole range of ka. The phenomena mentioned above hold qualitatively for any range of viscosity, although the shapes of the growth rate curves look different in Figs. 9(a) and 9(b) as higher viscosity shifts $\alpha^*_{\max}$ and $ka_{\max}$ toward significantly smaller values, i.e., a quantitative effect. When Oh>0, for $\tau=-1$ the growth rate increases with wavenumber but, after leveling off, it is almost bounded without ka_{cutoff} [see also Fig. 8(a)].

Figure 10 shows the dimensionless growth rate curves α^* as a function of dimensionless wave number ka, for m_0 to m_5, when Oh$=0$, for (a) $\tau=-1.01$ and (b) $\tau=-2$. The dimensionless anisotropic elasticity range corresponds to catastrophic instability mechanism (region II in Table I). The short wave instabilities are seen for all modes, but only six among all catastrophic modes are presented in the figure, clearly showing that lower modes grow faster than higher modes. In Figs. 10(a) and 10(b), the growth rate curves for m_0 to m_5 show the same pattern for $\tau=-1.01$ (just below the critically $\tau=-1$) and $\tau=-2$ (the thermodynamic limit), showing that the catastrophic instability for $\tau=-2$ grows much faster than that for $\tau=-1.01$ [see also Fig. 8(b)]. Further, it is shown that for $\tau<-1$ the ''lower'' ka_{cutoff} exist for the catastrophic modes only when $m\geqslant 2$, as explained in Eq. (46).

Figure 11 shows representative structures that summarize capillary instabilities in axial fibers (see Table I). Axial fibers display three types of linear instabilities, whose symmetry and existence are controlled by the magnitude and sign of the dimensionless surface anchoring energy τ. Large negative values of τ (region II) ignite catastrophic axisymmetric and nonaxisymmetric Hadamard instabilities, leading to fibrillation phenomena, as the effective surface tension coefficient $C_{\xi_{zz}}$ for curvature forces $f_{c,\xi_{zz}}$ is negative. Intermediate

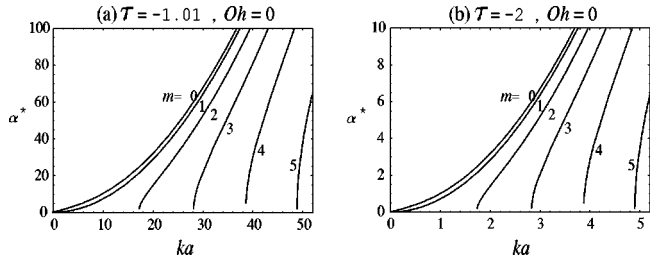

FIG. 10. Dimensionless growth rate curves α^* as a function of dimensionless wavenumber ka, for m_0 to m_5, when Oh$=0$, for (a) $\tau=-1.01$ and (b) $\tau=-2$. The dimensionless anisotropic elasticity range corresponds to catastrophic instability mechanism (region II in Table I): $\tau=-1.01$ (just below the criticality $\tau=-1$) and $\tau=-2$ (the thermodynamic limit).

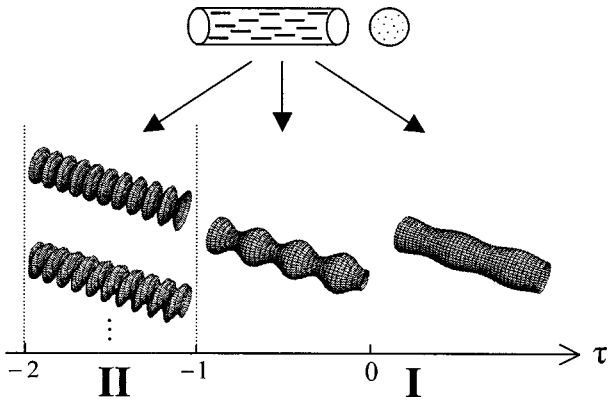

FIG. 11. Representative structures that summarize capillary instabilities in axial fibers (see Table I). Axial fibers display three types of linear instabilities, whose symmetry and existence are controlled by the magnitude and sign of the dimensionless anchoring energy τ. Varicose deformations emerge at positive and intermediate negative τ (region I) and surface fibrillation at large negative τ (region II).

negative values close to zero and positive values of τ (region I) lead to the axisymmetric Rayleigh instability, and to an eventual fiber break-up into droplets, because destabilizing displacement forces f_d overcome stabilizing curvature forces $f_{c,\xi_{zz}}$ and $f^{m0}_{c,\xi_{\theta\theta}}$, but $f^{m}_{c,\xi_{\theta\theta}}$. At the critical state of $\tau=-1$, the fiber instability is of catastrophic axisymmetric type. The only effect of viscosity is to slow the growth rate and increase the wavelength of the unstable modes.

IV. CONCLUSIONS

Capillary instabilities in nematic fibers reflect the anisotropic nature of liquid crystals. The surface elasticity of nematics contains orientation contributions that allow for the existence of bending stresses. Surface gradients of bending stresses provide additional anisotropic contributions to the capillary pressure of fibers that renormalize the classical displacement and curvature forces that exist in any fluid fiber. The exact nature and magnitude of the renormalization of the displacement and curvature forces depend on the nematic liquid crystal orientation and the anisotropic contribution to the surface energy. If the orientation is along the fiber axis, capillary instabilities may be axisymmetric or nonaxisymmetric, and if the anchoring energy strongly promotes normal (homeotropic) orientation to the surface, the usually stabilizing curvature forces become destabilizing and capillary instabilities with fibrillation phenomena arise. We are presently pursuing experimental verification of nonaxisymmetric capillary instability using rheological microscopy methods [32]. The phenomenology predicted in this paper is accessible, in principle, by changes in temperature, since the anchoring energy of a given interface is temperature dependent [7]. Thus, the classical fiber-to-droplet transformation is one of several possible instability pathways while others include surface fibrillation.

ACKNOWLEDGMENTS

This work was supported by the Air Force Office of Scientific Research, Mathematical and Space Science Program, under Grant No. F49620-00-1-0341. P. T. Mather acknowledges support from AFOSR, Chemistry and Life Sciences Division, Grant No. F49620-00-1-0100. One of us (A.C.) gratefully acknowledges partial financial support from McGill University.

[1] D. A. Edwards, H. Brenner, and D. T. Wasan, *Interfacial Transport Processes and Rheology* (Butterworths, Boston, 1989).
[2] V. G. Levich, *Physicochemical Hydrodynamics* (Prentice-Hall, Englewood Cliffs, NJ, 1962).
[3] J. C. Slattery, *Interfacial Transport Phenomena* (Springer-Verlag, New York, 1990).
[4] D. D. Edie and E. G. Stoner, in *Carbon-Carbon Materials and Composites*, edited by J. D. Buckley and D. D. Edie (Noyes, Park Ridge, NJ, 1993).
[5] A. D. Rey, Ind. Eng. Chem. Res. **36**, 1114 (1997).
[6] L. M. Blinov and V. G. Chigrinov, *Electrooptic Effects in Liquid Crystal Materials* (Springer-Verlag, New York, 1994).
[7] A. A. Sonin, *The Surface Physics of Liquid Crystals* (Gordon and Breach, Amsterdam, 1995).
[8] B. Jerome, Surface Alignment, in *Handbook of Liquid Crystals*, edited by D. Demus, J. Goodby, G. W. Gray, H.-W. Spiess, and V. Vill (Wiley-VCH, Weinheim, 1998), Vol. 1.
[9] H. Yokoyama, *Handbook of Liquid Crystal Research*, edited by P. J. Collins and J. S. Patel (Oxford University Press, New York, 1997).
[10] S. Chandrasekhar, *Liquid Crystals* (Cambridge University Press, Cambridge, 1992).
[11] T. J. Sluckin and A. Poniewierski, in *Fluid Interfacial Phenomena*, edited by C. A. Croxton (Wiley, Chichester, 1986).
[12] A. K. Sen and D. E. Sullivan, Phys. Rev. A **35**, 1391 (1987).
[13] S. Faetti, in *Physics of Liquid Crystalline Materials*, edited by I.-C. Khoo and F. Simoni (Gordon and Breach, Philadelphia, 1991).
[14] G. Barbero and G. Durand, in *Liquid Crystals in Complex Geometries*, edited by G. P. Crawford and S. Zumer (Taylor and Francis, London, 1996).
[15] J. L. Ericksen, in *Advances in Liquid Crystals*, edited by G. H. Brown (Academic, New York, 1979).
[16] E. G. Virga, *Variational Theories for Liquid Crystals* (Chapman Hall, London, 1994).
[17] A. D. Rey, Liq. Cryst. **26**, 913 (1999).
[18] A. D. Rey, J. Chem. Phys. **110**, 9769 (1999).
[19] J. T. Jenkins and P. J. Barrat, Q. J. Mech. Appl. Math. **27**, 111 (1974).

[20] C. Papenfuss and W. Muschik, Mol. Mater. **2**, 1 (1992).
[21] C. Pozrikidis, *Introduction to Theoretical and Computational Fluid Dynamics* (Oxford University Press, New York, 1997).
[22] P. G. de Gennes and J. Prost, *The Physics of Liquid Crystals* (Oxford University Press, London, 1993).
[23] H. Ehrentraut and S. Hess, Phys. Rev. E **51**, 2203 (1995).
[24] R. G. Larson, *The Structure and Rheology of Complex Fluids* (Oxford University Press, New York, 1999).
[25] A. D. Rey, J. Phys. II **7**, 1001 (1997).
[26] H. Q. Yang, Phys. Fluids A **4**, 681 (1992).
[27] E. Avital, Phys. Fluids **7**, 1162 (1995).
[28] X. Li, Atomization Sprays **5**, 89 (1995).
[29] A. D. Rey, Phys. Rev. E **61**, 1540 (2000).
[30] D. D. Joseph, *Fluid Dynamics of Viscoelastic Liquids* (Springer-Verlag, New York, 1990).
[31] S. Middleman, *Modeling Axisymmetric Flows: Dynamics of Films, Jets, and Drops* (Academic Press, San Diego, 1995).
[32] P. T. Mather, H. G. Jeon, C. D. Han, and S. Chang, Macromolecules **33**, 7594 (2000).